Configuration of the HERA Element

Aaron Parsons David DeBoer

August 25, 2015

1 Introduction

The design of the HERA element is driven by advances in our understanding of how an interferometer's chromatic response interacts with foreground emission to produce systematics in power spectral measurements of the 21cm reionization signal.

The basic architecture going in was a fixed zenith prime-focus paraboloid. The memo analyzes that structure in the context of a power spectrum measurement of the Epoch of Reionization.

2 Understanding Instrumental Chromaticity in the Context of the Wedge

For this discussion, we average the three-dimensional power spectrum $P(\mathbf{k})$ along a cylinder of $k_x^2 + k_y^2 = {k_\perp}^2$, where $\mathbf{k} \equiv (k_x, k_y, k_\parallel)$ is the three-dimensional wavevector, (k_x, k_y) are taken to be in the plane of the sky, and $k_\parallel$ is measured along the line-of-sight (spectral) direction. Recent work has shown that, for an interferometer whose analog bandpass and beam chromaticity are sufficiently smooth, systematics arising from foreground emission are isolated in the cylindrically averaged power spectrum $P(k_\perp, k_\parallel)$ within a wedge-shaped region , as derived analytically [Parsons et al., 2012b, Vedantham et al., 2012, Liu et al., 2014a,b], and confirmed in simulations [Datta et al., 2010, Hazelton et al., 2013] and observationally [Pober et al., 2013, Dillon et al., 2014, Parsons et al., 2014, Ali et al., 2015]:

$$\begin{aligned} |k_\parallel| &\leq \frac{X}{Y\nu} k_\perp + S/Y \\ &\leq \frac{b}{Yc} + S/Y, \end{aligned} \tag{1}$$

where X, Y are cosmological scalars relating angular size and spectral frequency to comoving physical size, respectively, ν is spectral frequency, and $b = |\mathbf{b}|$ is the magnitude of the baseline vector for antennas in an interferometric pair, which substitutes for $k_\perp$ according to the relation $\mathbf{k}_\perp = \nu \mathbf{b}/(Xc)$. As we will derive below, S is an additional additive delay offset related to the combined spectral smoothness of foregrounds and the antenna response.

As pointed out in Parsons et al. [2012b], the factor of b/c in the second line of equation (1) can be interpreted as the light-crossing time or maximum geometric signal delay, $\tau_{b,max}$ associated with an interferometric baseline. Particularly for per-baseline analyses such as those employed on PAPER [Parsons et al., 2014, Jacobs et al., 2015, Moore et al., 2015, Ali et al., 2015], *signal*

delay turns out to be a powerful basis for understanding the chromatic effects of interferometric observations. Signal delay arises as the Fourier dual to spectral frequency, according to the delay transformation of a visibility,

$$\tilde{V}_{\mathbf{b}}(\tau) = \int d\nu \; V_{\mathbf{b}}(\nu) e^{2\pi i \tau \nu}. \tag{2}$$

The measurement equation defines the visibility as

$$V_{\mathbf{b}}(\nu) = \int d\Omega \; A(\hat{s}, \nu) \; I(\hat{s}, \nu) e^{-2\pi i \frac{\mathbf{b}\cdot\hat{s}}{c}\nu}, \tag{3}$$

where A is the antenna response as a function of directon $\hat{s}$ and I is the sky intensity. We define the geometric signal delay in direction $\hat{s}$ as $\tau_{\mathbf{b},\hat{s}} \equiv \mathbf{b}\cdot\hat{s}/c$ in order to re-express the delay-transformed visibility as

$$\begin{aligned}\tilde{V}_{\mathbf{b}}(\tau) &= \iint d\nu \; d\Omega \; A(\hat{s}, \nu) \; I(\hat{s}, \nu) e^{-2\pi i \nu (\tau_{\mathbf{b},\hat{s}} - \tau)} \\ &= \int d\Omega \; \tilde{A}(\hat{s}, \tau) * \tilde{I}(\hat{s}, \tau) * \delta_D(\tau_{\mathbf{b},\hat{s}} - \tau),\end{aligned} \tag{4}$$

where δ_D is the Dirac delta function, '˜' signifies Fourier transformation along the frequency axis, and '$*$' denotes convolution.

Under the "delay approximation" [Parsons et al., 2012b], signal delay τ can be interpreted as a reasonable approximation to $k_\parallel$, giving us the following relationship between the delay-transformed visibility and the power spectrum:

$$\tilde{V}^2_{\mathbf{b}}(\tau) \approx \left(\frac{2k_B}{\lambda^2}\right)^2 \frac{\Omega B}{X^2 Y} \widehat{P}(\mathbf{k}_\perp, k_\parallel), \tag{5}$$

where k_B is Boltzmann's constant, λ is spectral wavelength, Ω is the angular area of the power-squared beam [Parsons et al., 2014], and B is the effective bandwidth over which the delay transformation is performed.

We can now revisit the bound on systematics arising from the interaction of foreground emission and instrumental chromaticism given in equation (1). Let us assume for a moment that A and I are perfectly flat functions of frequency, so that $\tilde{A}$ and $\tilde{I}$ are delta functions centered at $\tau = 0$. In this case, the value of $\tilde{V}_{\mathbf{b}}(\tau)$ is determined by the integral over $\tilde{A}(\hat{s}, 0)\; \tilde{I}(\hat{s}, 0)$ in the sky directions that satisfy $\tau_{\mathbf{b},\hat{s}} = \tau$. For a given baseline $\mathbf{b} = \mathbf{k}_\perp (Xc/\nu)$, $\tau_{\mathbf{b},\hat{s}}$ is bounded by $\tau_{b,max} = b/c$, implying that for the case we have outlined, $\tilde{V}_{\mathbf{b}}(\tau)$ must be zero outside of a region $|\tau| \leq b/c$. Under the delay approximation, $k_\parallel \approx \tau/Y$, so we can use equation (5) and say that $P(k_\perp, k_\parallel)$ must be zero outside of the region specified in equation (1) for $S = 0$.

The inclusion of S in equation (1) accounts for precisely the terms we neglected above: the spectral structure in A and I, or more precisely, the delay-domain width of

$$\langle \tilde{A} * \tilde{I} \rangle(\tau) \equiv \int d\Omega \; \tilde{A}(\hat{s}, \tau) * \tilde{I}(\hat{s}, \tau), \tag{6}$$

where $\langle \dots \rangle$ denotes the average over solid angle. In order to determine S quantitatively, however, we must clarify what is the relevant width in delay-domain. The purpose of equation (1) is to illustrate the boundary between the systematics-dominated and signal-dominated regimes. As such, it makes

the most sense to determine width by the interval in delay domain outside of which $\langle \tilde{A} * \tilde{I} \rangle(\tau)$ is below the expected level of the 21cm reionization signal. Spectrally smooth ($\tau \approx 0$) foregrounds are approximately four to five times brighter that the expected reionization signal [Santos et al., 2005, Ali et al., 2008, de Oliveira-Costa et al., 2008, Jelić et al., 2008, Bernardi et al., 2009, 2010, Ghosh et al., 2011], so a conservative definition of S requires

$$\frac{|\langle \tilde{A} * \tilde{I} \rangle(\tau)|}{|\langle \tilde{I} \rangle(\tau = 0)|} < 10^{-6}. \tag{7}$$

In words, we define S as the delay interval over which $\langle \tilde{A} * \tilde{I} \rangle$ falls off by -60 dB. At this level, the contribution from antenna systematics arising from bright foregrounds are below the expected signal level.

Given this framework, an obvious design goal for an interferometer aiming to measure the 21cm reionization signal is create antennas that can be close-packed to minimize b, and which yield an antenna response that minimizes S. However, as we will explore in more detail below, these goals must be balanced against cost.

2.1 Inherent Chromaticity of Foregrounds

Before we explore antenna design, however, it would be convenient to set an upper bound on the contribution of $\tilde{I}$ in equation (7). The result is strongly dependent on windowing, however choosing a Blackman-Harris window and playing with power-law spectral indices of -1 and -2, we find that a width for $\tilde{I}$ in range of 10 to 60 ns provides a reasonable bound. This suggests diminishing returns associated with pushing instrumental chromaticity much lower than 10 to 60 ns.

Also, as we push antennas closer together, galactic synchrotron emission (our dominant foreground) gets brighter as $C_\ell \propto \ell^{-2.4}$ [Tegmark et al., 2000, Santos et al., 2005]. Under the assumption that $k_\parallel$ is the dominant component of $\mathbf{k}$ (which holds for the short baselines used in PAPER and HERA), this implies that $|\langle \tilde{A} * \tilde{I} \rangle(\tau)|^2$ must decrease more rapidly than τ^{-3} for a reduction in baseline length to result in a reduction in foreground contamination at a given $k_\parallel$ scale. Hence, the combined chromaticity of the antenna beam and the galactic synchrotron foreground set an effective minimum baseline length, shorter than which foreground systematics no longer decrease, and could even potientially extend further in $|k_\parallel|$. This departure from the strictly linear relationship in equation (1) (which we will call the "ankle") for the shortest baselines is a telltale sign of the influence of diffuse synchrotron emission.

Figure 3 in Pober et al. [2013] shows evidence of the departure equation (1) described above for baselines shorter than $\lesssim 10$ wavelengths. Although this empirical result includes a contribution from the PAPER antenna beam, the constant additive term that $\tilde{A}$ contributes (which is baseline dependent) to the wedge boundary does not change the position of the ankle. Also worth noting is that, although an ankle appears around ~ 9 wavelengths, the extent of the wedge in $k_\parallel$ continues to decrease slowly toward even shorter baselines. This implies that, while there are diminishing returns in foreground systematics for using baseline shorter than ~ 18 m (9 wavelengths at 150 MHz), there does not appear to be a strong penalty for doing so either.

2.2 Antenna Chromaticity

So far, we have largely ignored the contribution of the antenna term in $\langle \tilde{A} * \tilde{I} \rangle(\tau)$. We now have a handle on the chromaticism introduced by the baseline term in equation (3) and an indication of

when shorter baselines stop linearly reducing the occupancy of foreground systematics in $|k_\parallel|$. As we argued above, $b \lesssim 20$ m is an approximate threshold for when the chromaticity of the baseline term is no longer dominant. This suggests that foreground systematics are unlikely to drop below a width in delay domain corresponding to $b/c \sim 60$ ns ($|k_\parallel| \sim 0.03h$ Mpc^{-1} at 150 MHz).

Therefore, a reasonable specification for an interferometer targeting 21cm power spectrum measurements and working outside the wedge to avoid foregrounds might be to equally partition a chromaticity budget (i.e. delay-domain width) between the baseline term $\delta_D(\tau_{\mathbf{b},\hat{s}} - \tau)$, the inherent foreground term $\tilde{I}(\hat{s}, \tau)$, and the antenna term $\tilde{A}(\hat{s}, \tau)$. As described in equation (7), the relevant delay domain width is measured at the -60 dB point. Therefore, the specification we set for the chromaticity of the antenna is

$$\frac{|\langle \tilde{A} \rangle(\hat{s}, \tau = 60 \text{ ns})|}{|\tilde{\langle A \rangle}(\hat{s}, \tau = 0 \text{ ns})|} < 10^{-6}. \tag{8}$$

Here, we have separated the antenna and sky terms in $\langle \tilde{A} * \tilde{I} \rangle(\tau)$ in order to set a specification for the antenna term alone.

Under this specification, we assume the final chromaticity (wedge width) to be the sum of the individual widths of the $\tilde{A}$, $\tilde{I}$, and $\delta_D(\tau_{\mathbf{b},\hat{s}} - \tau)$ terms, for a total of 180 ns ($|k_\parallel| = 0.9h$ Mpc^{-1} at 150 MHz).

3 HERA Element Design

As shown above, the delay-spectrum analysis technique employed for HERA requires that foreground systematics be tightly bounded within a wedge-shaped region in $(k_\perp, k_\parallel)$ space, such that contamination outside of this region falls below the expected level of the 21cm reionization signal. The supplied value from the analysis team is that reflections must be reduced by at least -60 dB at 60 ns. Another formulation is VSWR < 1.002 integrated over fluctuation scales of $\Delta\nu \leq 17$ MHz.

Assuming that HERA elements will have to deliver substantially more collecting area per feed than the current PAPER design, we adopted a parametrizable design based on a parabolic dish with a feed suspended over it. Thus, the optics of the HERA dish is set by three factors:

1. meeting the chromaticity specification of -60 dB at 60 ns, (Eq. 8)
2. minimizing the impact of baseline-coupling systematics, and
3. minimizing cost for a fixed sensitivity

The relevant parameters are the diameter (D), the focal length (f) and the overall sensitivity (essentially, N, the total number of elements). Antenna chromaticity is largely determined by the focal length (at least as a design parameter), and the discussion will focus on that.

3.1 Focal Length

Optimizing the focal length comes down to simultaneously optimizing the f/D for system performance and f for delay performance (chromaticity). We discuss both of these aspects below.

3.1.1 Efficiency

Assuming a feed based on the PAPER design for a backplane without flaps, we computed a series of analytical models at 150 MHz versus diameter over a 3.4–4.6 m range in focal height for an ideal parabolic dish. These models were used to determine the total efficiency of feed/reflector system, with efficiency η computed as the effective collecting area relative to the total geometric collecting area of a circular aperture of the indicated diameter. As shown in Figure 1, model efficiencies peak at $\eta \approx 0.73$ for focal ratios of $f/D \approx 0.32$ (the solid lines with the x-axis divided by 10), largely independent of the absolute scale of diameter.

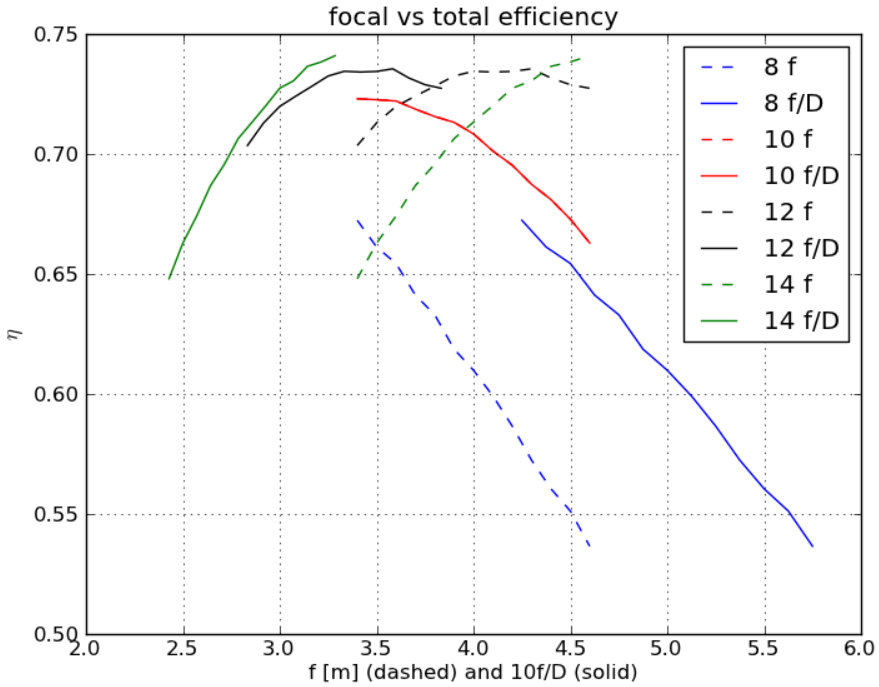

Figure 1: The model efficiency of a PAPER feed suspended over an ideal parabolic dish. The dashed curves indicate the efficiencies over a 3.4–4.6 m range in focal height f for the dish diameters D indicated in the legend. The solid curves extrapolate the model efficiencies of the corresponding dashed curves to a $D = 10$ m dish (note the red dashed and solid curves are identical). The approximate agreement of the solid curves indicates that to first order, efficiency is a function of the focal ratio f/D. The absolute scaling of η with D appears as a second-order (few percent) increase in efficiency. Hence, peak efficiencies of order $\eta \approx 0.73$ are expected for focal ratios of $f/D \approx 0.32$.

3.1.2 Chromatic Effects

The dominant source of chromaticism within the antenna can be identified with internal signal reflections, with delays set largely by the focal length. Diffraction around dish edges and the evolving response of the feed also introduce chromaticism, but the scale of these frequency-dependent

effects are expected to be significantly broader than the specified 17 MHz scale. In order to be problematic, signal reflections originating at the feed must re-enter the feed after a time delay of 60 ns before they are attenuated by 60 dB.Taking a geometric interpretation for an ideal paraboloid, off-axis emission from the feed is reflected out to the sky without re-entering the feed.Therefore, the dominant source of reflections is expected to arise between the feed and vertex.If reflections between the feed and vertex are dominant, as noted above, the most important determinant of the timescale of reflections will be the feed height above the vertex.

Here, we adopt the focal ratio of $f/D = 0.32$ derived in the previous section in the context of maximizing efficiency. In doing so, we reduce the parametrization of our parabolic dish to a single degree of freedom: the diameter D (or, equivalently f). We may then explore how the timescale and amplitude of reflections between the feed and the vertex of the paraboloid scale with D. As a tool for determining coarse scaling relationships we will use a geometric (far-field) model.

Geometrically, waves arriving at the feed from the sky absorbed and reflected in accordance with the impedance match between free space and the feed/balun system. The reflected wave is essentially re-emitted from the feed into the dish, and bulk of it is reflected back to the sky. However, as discussed previously, emission toward the the vertex of the parabola may be reflected back toward the feed, whereupon the absorption/reflection process repeats with an attenuated amplitude.

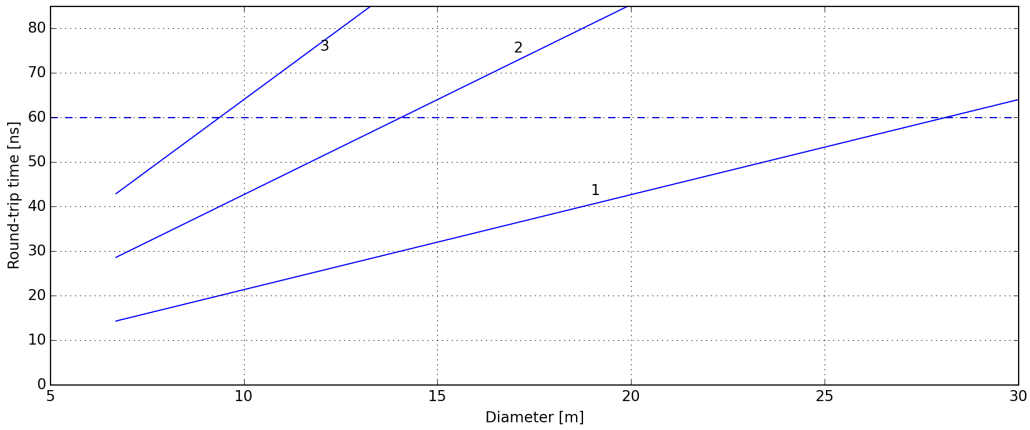

Figure 2: Round-trip propagation times between feed and vertex for $f/D = 0.32$, shown for 1, 2, and 3 reflections. The 60-ns timescale appearing in the specification is indicated with a dashed line.

We begin by computing the round-trip light-propagation times between the vertex and feed. Figure 2 shows the resulting signal delay for reflections spanning 1, 2 and 3 round trips. To interpret the results, let us explore different cases. If we assume that after two reflections, the reflected signal has been attenuated below the -60 dB threshold in the specification, then the first reflection (which is above the threshold) must have a timescale shorter than 60 ns. Following the curve for 1 round-trip reflection, we see that a 28-m dish (with a focal height of ~ 9 m) is the maximum size that would meet the specification. If, on the other hand, a 60 dB attenuation is only achieved on the third reflection, then the curve for 2 round trips suggests a maximum diameter of 14 m. Similarly, requiring the attenuation associated with one more reflection moves the maximum diameter down

to 9.4 m.

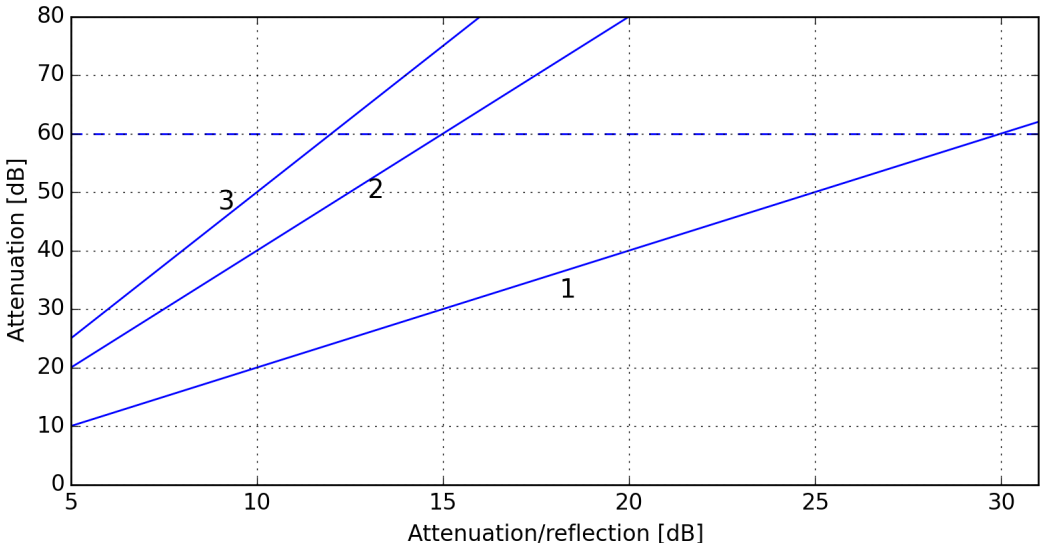

Figure 3: Overall attenuation for 1, 2 and 3 trips.

Finally, we may ask, given the number of reflections that fall inside of 60 ns, what is the attenuation per reflection Γ that puts the signal level below -60 dB after 60 ns? Here, Γ includes all loss factors, including the reflection coefficient associated with the impedance match of the feed, path loss, etc. Illustrated in Figure 3 is the total attenuation of a signal arriving at timescales <60 ns, given as a function of Γ for the indicated number of reflections falling inside 60 ns.

Combining the results in Figures 2 and 3, we can see that dishes with $D < 9.4$ m must have $\Gamma < -12$ dB, dishes where 9.4 m $< D <$ 14 m require $\Gamma < -15$ dB, and those with diameters 14 m $< D <$ 28 m need $\Gamma < -30$ dB.

It is worth noting that imperfect impedance matches in the feed as a function of frequency generally place the reflection coefficient of the feed itself in the range of -5 to -15 dB. We must rely on directing reflected waves away from the feed to achieve the total attenuation per reflection that is required. Geometrically, we can estimate that for a parabolic reflector that reflects emission from the feed straight upward, a wave must intersect the paraboloid at a distance of half a wavelength off axis to avoid passing close enough to the feed to be re-absorbed. Assuming $\lambda = 2$ m, this angle is

$$\phi \approx \tan^{-1} \frac{1}{f}. \tag{9}$$

For a 14-m dish with a focal ratio of $f/D = 0.32$ ($f \approx 4.5$ m), $\alpha \approx 13°$. This gives a solid angle of 0.15 sr into which the feed must emit in order to receive the reflection. We can calculate the power emitted into this region numerically given a model of the feed response, but coarsely, for a feed emitting uniformly into 2π sr, the power emitted into this region represents -16 dB of the total reflected power. Thus, it seems likely that $\Gamma \sim -15$ dB is achievable, while $\Gamma \sim -30$ dB would require very careful tuning of the feed and dish, if possible at all.

A full prototype has been built to investigate construction methods and to test the standing wave specification. Using a network analyzer and a modified feed, this was measured as shown

in Fig. 4. The frequency sweep used was 50 MHz to 1 GHz, which exceeds the feed bandwidth. Even so, the 60 dB at 60 ns specification is nearly met. These tests will be retaken using a nearly completed element in Green Bank.

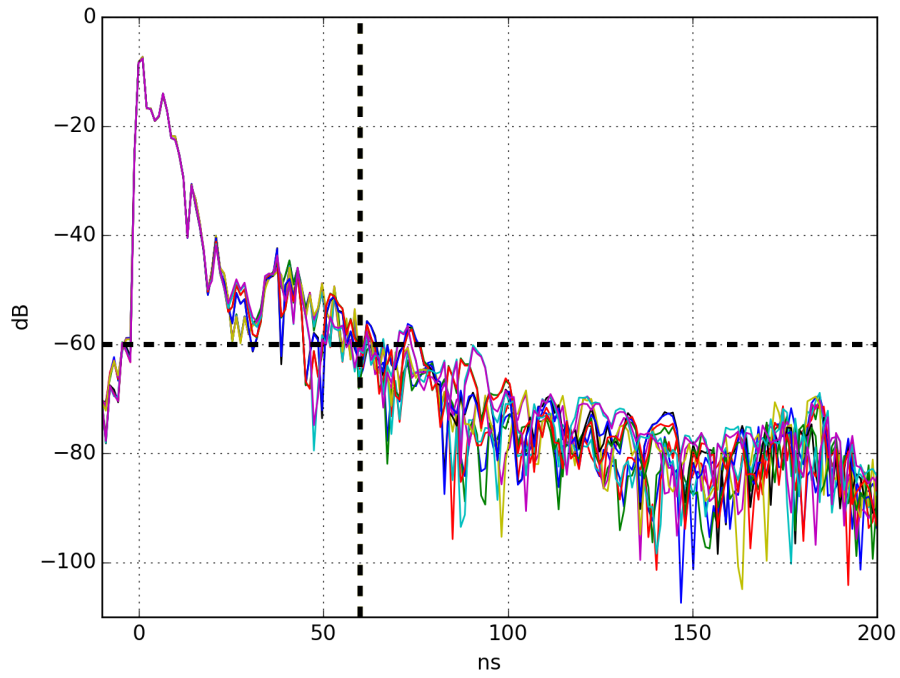

Figure 4: Network analyzer reflection measurements on prototype dish under several different configurations. The dashed show the specification "60 by 60".

4 Cross-Coupling

As described above, minimizing internal reflections that introduce signal delays is the primary design requirement of the HERA dish. A secondary consideration is the reduction of cross-coupling between the feeds of adjacent dishes. Since the focus of the parabolic dish lies above the rim, feeds potentially have a direct line of sight to one another. Noise and signal reflections emanating from one feed and coupling into another can introduce spurious correlations that show up, to first order, as a static (zero fringe rate) additive phase term with significant spectral structure.

Although current PAPER analysis removes such static correlations via fringe-rate filtering, this approach limits observing to regions away from the celestial poles, and significantly reduces the number of independent sky samples obtained with a given baseline. Although this approach may remain an imporant tool for dealing with feed cross-coupling, it would be nice to limit its necessity. One obvious way to do this is to shield feeds from one another.

To achieve this, the HERA dish design incorporates mesh screens at the boundaries of dishes that rise high enough to shield feeds from one another. In the limit of geometric optics, these screens

perfectly isolate feeds from one another, but risk introducing a new internal reflection pathway. To avoid reflecting signals back into the feed, screens may be tilted such that a ray originating from the feed and arriving at the screen are reflected upward far enough that they miss the feed by a wavelength. For a dish with a radius of $\sim$ 7 m and an observing wavelength of $\sim$2 m, this requires a tilt angle α given by $\tan\alpha = 1/7$. Thus, in the geometric limit, shielding screens must be approximately 8 degrees off of vertical.

In practice, the geometric optical limit is not met, and the above specification can only be a coarse rule of thumb. Most notably, the top edge of the screen will introduce diffraction that degrades feed-feed isolation. Scalloping or rolling the edges of screens may help reduce diffraction, but these ideas will need to be tested in the field to show their efficacy.

Pending field testing, HERA dishes are designed to include screens that rise $\sim$ 2 m from the rim ($\sim$0.75 m above the feeds), supported by the same large wooden poles that are used to suspend the feed. The bottom of these screens are held at a distance of 30 cm inward relative to the top, for a tilt of 8.5 degrees from vertical.

5 Sensitivity and Cost

The equation for sensitivity has been described in previous works (*c.f* Parsons et al. [2012a],Pober et al. [2014],) and depends on many parameters related to the instrumentation, the configuration, the location, the observing strategy, etc. A useful form for the proposed compact configuration is Eq 27 in Parsons et al. [2012a] and reproduced here:

$$\begin{aligned}\Delta^2_N(k) \approx 60 &\left[\frac{k}{0.1h\mathrm{Mpc}^{-1}}\right]^{\frac{5}{2}} \left[\frac{6\mathrm{MHz}}{B}\right]^{\frac{1}{2}} \left[\frac{1}{\Delta \ln k}\right]^{\frac{1}{2}} \\ &\times \left[\frac{\Omega}{0.76\mathrm{sr}}\right] \left[\frac{T_{\mathrm{sys}}}{500\mathrm{K}}\right]^2 \left[\frac{6\mathrm{hrs}}{t_{\mathrm{per\_day}}}\right]^{\frac{1}{2}} \\ &\times \left[\frac{120\mathrm{days}}{t_{\mathrm{cam}}}\right] \left[\frac{32}{N_a}\right] \left[\frac{10^4 f_o}{f}\right]^{\frac{1}{2}} \mathrm{mK}^2\end{aligned} \tag{10}$$

where k is the magnitude of the k-mode, B is the bandwidth, $\Delta \ln k$ is the log of the binsize, Ω is the field-of-view, T_{sys} is the system temperature, $t_{\mathrm{per\_day}}$ is the number of hours observed per day, t_{cam} is the number of days observed, N_a is the number of antennas, and f_o/f is a configuration metric for a redundant array as therein defined.

Note that $\Delta^2_N(k)$ is the standard radiometric sensitivity equation, scaled by the volume in k-space, normalized by the power spectrum Fourier coefficient, and reduced by the number of independent samples in a given k-mode bin, which may have both coherent and incoherent application.

Pulling out terms relating to diameter (D_a) and number, we can write Eq. 10 as

$$\Delta^2_N(k) \propto \frac{\Omega\sqrt{f_o/f}}{N_a\sqrt{t_{\mathrm{per\_day}}}} \propto \frac{(1/D_a^2)(1/\sqrt{N_a})}{N_a/\sqrt{D_a}} = D_a^{-\frac{3}{2}} N_a^{-\frac{3}{2}} \tag{11}$$

where the dependencies on diameter and number have been substituted in, noting that the expressions for f_o/f and $t_{\mathrm{per_day}}$were derived in Parsons et al. [2012b] where the baselines for the close-packed array are multiples of the diameter. Letting the reduced sensitivity be $C = D_a N_a$

and scaling for canonical values of $D_a = 14$ m, $N_a = 331$ m, the needed number of antennas as a function of diameter (shown in Figure 5 left) is

$$N_a = 4634/D_a \tag{12}$$

Though approximations, these results agree with simulations of HERA performance for a wide range of N_a, D_a and k values ([Pober et al., 2014]). This analysis differs somewhat from others (*e.g.* Mellema et al. [2013]) since it explicitly incorporates use of redundant baselines to achieve better sensitivities.

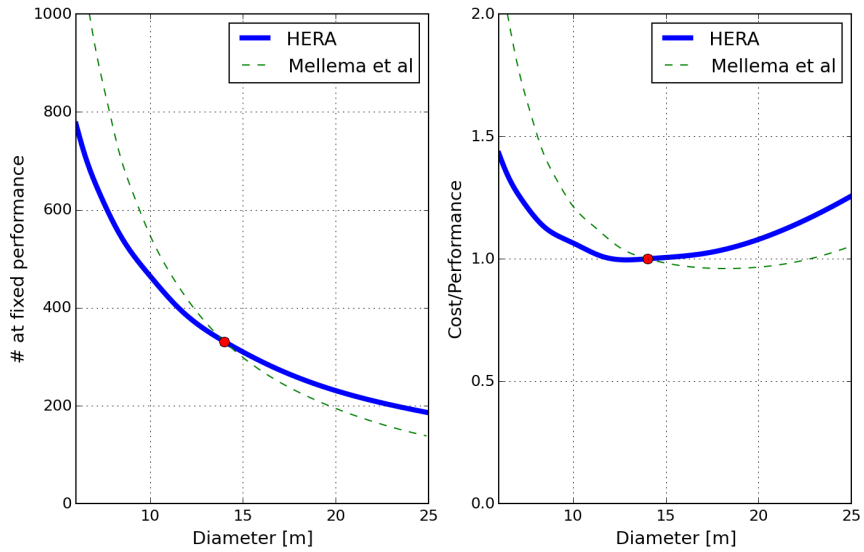

Figure 5: (Left) Number of antennas at fixed sensitivity with reference of 331 14-m antennas. (Right) Cost/performance analysis for HERA. The red circle indicates the reference 14-meter design.

The sensitivity specification is to maximize performance per cost, which determines the element diameter (D_a) and the number of elements (N_a) subject to the constraints above. One therefore needs a model of cost and performance as a function of D_a and N_a. Given a fairly mature element and system design, a bottoms-up costing appropriate for element diameters from about 6-m to 30-m has been done for hex-numbers corresponding to element counts from 91 to 1141. The costs here are only those associated with delivering the array to that scope on-site, so excluding development and science. The results are shown in Fig. 5 (right).

6 Construction Implications

The element construction consists of radial spars with mesh laid over top, so the optics aren't truly a paraboloid, but rather a "faceted" parabola. In order to determine how many spars are needed, the rms of idealized versions was computed for 12 and 24 spars, as shown in Fig. 6 (left two panels). The 12-spar rms deviation from a paraboloid is 4.6 cm, which corresponds to a Ruze

efficiency of 83.4% at 220 MHz. The 24-spar values are 1.2cm and 98.8 %, however 24 spars get difficult to accommodate with a reasonably sized hub. Since 12 spars are not adequate and 24 spars gets crowded a "hybrid" 12-spar-to-24-spar antenna has been designed (right-most panel of Fig. 6). This approach yields an rms of 1.2cm and a Ruze efficiency of 98.7% and also accommodates the natural panel-sized width of commercial screen material.

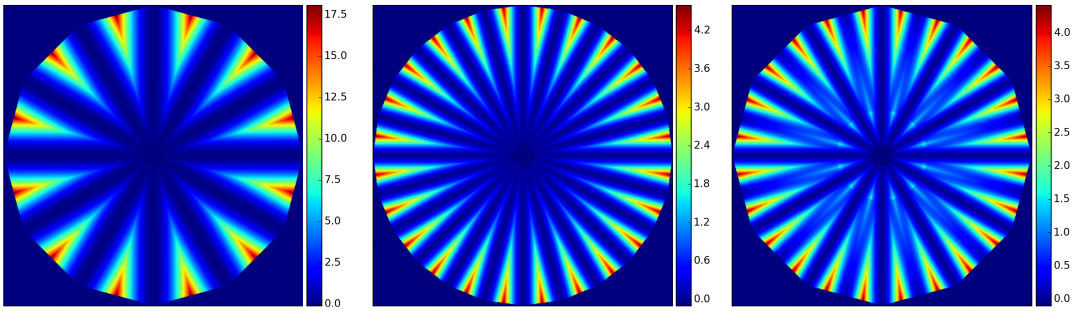

Figure 6: Deviations of a "faceted parabola" from a true paraboloid in cm. From left to right are models using 12 spars (rms=4.6cm, Ruze@220 MHz=83.4%), 24 spars (1.2, 98.8%) and the 12/24 hybrid (1.2, 98.7%).

References

S. S. Ali, S. Bharadwaj, and J. N. Chengalur. Foregrounds for redshifted 21-cm studies of reionization: Giant Meter Wave Radio Telescope 153-MHz observations. **??***jnlMNRAS*, 385:2166–2174, April 2008. doi: 10.1111/j.1365-2966.2008.12984.x.

Z. S. Ali, A. R. Parsons, H. Zheng, J. C. Pober, A. Liu, J. E. Aguirre, R. F. Bradley, G. Bernardi, C. L. Carilli, C. Cheng, D. R. DeBoer, M. R. Dexter, J. Grobbelaar, J. Horrell, D. C. Jacobs, P. Klima, D. H. E. MacMahon, M. Maree, D. F. Moore, N. Razavi, I. I. Stefan, W. P. Walbrugh, and A. Walker. PAPER-64 Constraints on Reionization: The 21cm Power Spectrum at z=8.4. *ArXiv e-prints*, February 2015.

G. Bernardi, A. G. de Bruyn, M. A. Brentjens, B. Ciardi, G. Harker, V. Jelić, L. V. E. Koopmans, P. Labropoulos, A. Offringa, V. N. Pandey, J. Schaye, R. M. Thomas, S. Yatawatta, and S. Zaroubi. Foregrounds for observations of the cosmological 21 cm line. I. First Westerbork measurements of Galactic emission at 150 MHz in a low latitude field. **??***jnlA&A*, 500:965–979, June 2009. doi: 10.1051/0004-6361/200911627.

G. Bernardi, A. G. de Bruyn, G. Harker, M. A. Brentjens, B. Ciardi, V. Jelić, L. V. E. Koopmans, P. Labropoulos, A. Offringa, V. N. Pandey, J. Schaye, R. M. Thomas, S. Yatawatta, and S. Zaroubi. Foregrounds for observations of the cosmological 21 cm line. II. Westerbork observations of the fields around 3C 196 and the North Celestial Pole. **??***jnlA&A*, 522:A67+, November 2010. doi: 10.1051/0004-6361/200913420.

A. Datta, J. D. Bowman, and C. L. Carilli. Bright Source Subtraction Requirements for Redshifted 21 cm Measurements. *ApJ*, 724:526–538, November 2010. doi: 10.1088/0004-637X/724/1/526.

A. de Oliveira-Costa, M. Tegmark, B. M. Gaensler, J. Jonas, T. L. Landecker, and P. Reich. A model of diffuse Galactic radio emission from 10 MHz to 100 GHz. **??***jnlMNRAS*, 388:247–260, July 2008. doi: 10.1111/j.1365-2966.2008.13376.x.

J. S. Dillon, A. Liu, C. L. Williams, J. N. Hewitt, M. Tegmark, E. H. Morgan, A. M. Levine, M. F. Morales, S. J. Tingay, G. Bernardi, J. D. Bowman, F. H. Briggs, R. C. Cappallo, D. Emrich, D. A. Mitchell, D. Oberoi, T. Prabu, R. Wayth, and R. L. Webster. Overcoming real-world obstacles in 21 cm power spectrum estimation: A method demonstration and results from early Murchison Widefield Array data. **??***jnlPhys. Rev. D*, 89(2):023002, January 2014. doi: 10.1103/PhysRevD.89.023002.

A. Ghosh, S. Bharadwaj, S. S. Ali, and J. N. Chengalur. Improved foreground removal in GMRT 610 MHz observations towards redshifted 21-cm tomography. **??***jnlMNRAS*, 418:2584–2589, December 2011. doi: 10.1111/j.1365-2966.2011.19649.x.

B. J. Hazelton, M. F. Morales, and I. S. Sullivan. The Fundamental Multi-baseline Mode-mixing Foreground in 21 cm Epoch of Reionization Observations. *ApJ*, 770:156, June 2013. doi: 10.1088/0004-637X/770/2/156.

D. C. Jacobs, J. C. Pober, A. R. Parsons, J. E. Aguirre, Z. S. Ali, J. Bowman, R. F. Bradley, C. L. Carilli, D. R. DeBoer, M. R. Dexter, N. E. Gugliucci, P. Klima, A. Liu, D. H. E. MacMahon,

J. R. Manley, D. F. Moore, I. I. Stefan, and W. P. Walbrugh. Multiredshift Limits on the 21 cm Power Spectrum from PAPER. *ApJ*, 801:51, March 2015. doi: 10.1088/0004-637X/801/1/51.

V. Jelić, S. Zaroubi, P. Labropoulos, R. M. Thomas, G. Bernardi, M. A. Brentjens, A. G. de Bruyn, B. Ciardi, G. Harker, L. V. E. Koopmans, V. N. Pandey, J. Schaye, and S. Yatawatta. Foreground simulations for the LOFAR-epoch of reionization experiment. **??***jnlMNRAS*, 389: 1319–1335, September 2008. doi: 10.1111/j.1365-2966.2008.13634.x.

Adrian Liu, Aaron R. Parsons, and Cathryn M. Trott. Epoch of reionization window. i. mathematical formalism. *Phys. Rev. D*, 90:023018, Jul 2014a. doi: 10.1103/PhysRevD.90.023018. URL `http://link.aps.org/doi/10.1103/PhysRevD.90.023018`.

Adrian Liu, Aaron R. Parsons, and Cathryn M. Trott. Epoch of reionization window. ii. statistical methods for foreground wedge reduction. *Phys. Rev. D*, 90:023019, Jul 2014b. doi: 10.1103/PhysRevD.90.023019. URL `http://link.aps.org/doi/10.1103/PhysRevD.90.023019`.

G. Mellema, L. V. E. Koopmans, F. A. Abdalla, G. Bernardi, B. Ciardi, S. Daiboo, A. G. de Bruyn, K. K. Datta, H. Falcke, A. Ferrara, I. T. Iliev, F. Iocco, V. Jelić, H. Jensen, R. Joseph, P. Labroupoulos, A. Meiksin, A. Mesinger, A. R. Offringa, V. N. Pandey, J. R. Pritchard, M. G. Santos, D. J. Schwarz, B. Semelin, H. Vedantham, S. Yatawatta, and S. Zaroubi. Reionization and the Cosmic Dawn with the Square Kilometre Array. *Experimental Astronomy*, 36:235–318, August 2013.

D. Moore, J. E. Aguirre, A. Parsons, Z. Ali, R. Bradley, C. Carilli, D. DeBoer, M. Dexter, N. Gugliucci, D. Jacobs, P. Klima, A. Liu, D. MacMahon, J. Manley, J. Pober, I. Stefan, and W. Walbrugh. New Limits on Polarized Power Spectra at 126 and 164 MHz: Relevance to Epoch of Reionization Measurements. *ArXiv e-prints*, February 2015.

A. Parsons, J. Pober, M. McQuinn, D. Jacobs, and J. Aguirre. A Sensitivity and Array-configuration Study for Measuring the Power Spectrum of 21 cm Emission from Reionization. *ApJ*, 753:81, July 2012a. doi: 10.1088/0004-637X/753/1/81.

A. R. Parsons, J. C. Pober, J. E. Aguirre, C. L. Carilli, D. C. Jacobs, and D. F. Moore. A Per-baseline, Delay-spectrum Technique for Accessing the 21 cm Cosmic Reionization Signature. *ApJ*, 756:165, September 2012b. doi: 10.1088/0004-637X/756/2/165.

A. R. Parsons, A. Liu, J. E. Aguirre, Z. S. Ali, R. F. Bradley, C. L. Carilli, D. R. DeBoer, M. R. Dexter, N. E. Gugliucci, D. C. Jacobs, P. Klima, D. H. E. MacMahon, J. R. Manley, D. F. Moore, J. C. Pober, I. I. Stefan, and W. P. Walbrugh. New Limits on 21 cm Epoch of Reionization from PAPER-32 Consistent with an X-Ray Heated Intergalactic Medium at z = 7.7. *ApJ*, 788:106, June 2014. doi: 10.1088/0004-637X/788/2/106.

J. C. Pober, A. R. Parsons, J. E. Aguirre, Z. Ali, R. F. Bradley, C. L. Carilli, D. DeBoer, M. Dexter, N. E. Gugliucci, D. C. Jacobs, P. J. Klima, D. MacMahon, J. Manley, D. F. Moore, I. I. Stefan, and W. P. Walbrugh. Opening the 21 cm Epoch of Reionization Window: Measurements of Foreground Isolation with PAPER. **??***jnlApJ*, 768:L36, May 2013. doi: 10.1088/2041-8205/768/2/L36.

J. C. Pober, A. Liu, J. S. Dillon, J. E. Aguirre, J. D. Bowman, R. F. Bradley, C. L. Carilli, D. R. DeBoer, J. N. Hewitt, D. C. Jacobs, M. McQuinn, M. F. Morales, A. R. Parsons, M. Tegmark, and D. J. Werthimer. What Next-generation 21 cm Power Spectrum Measurements can Teach us About the Epoch of Reionization. *ApJ*, 782:66, February 2014. doi: 10.1088/0004-637X/782/2/66.

M. G. Santos, A. Cooray, and L. Knox. Multifrequency Analysis of 21 Centimeter Fluctuations from the Era of Reionization. *ApJ*, 625:575–587, June 2005. doi: 10.1086/429857.

M. Tegmark, D. J. Eisenstein, W. Hu, and A. de Oliveira-Costa. Foregrounds and Forecasts for the Cosmic Microwave Background. *ApJ*, 530:133–165, February 2000. doi: 10.1086/308348.

H. Vedantham, N. Udaya Shankar, and R. Subrahmanyan. Imaging the Epoch of Reionization: Limitations from Foreground Confusion and Imaging Algorithms. *ApJ*, 745:176, February 2012. doi: 10.1088/0004-637X/745/2/176.